Al-Azhar Bulletin of Science

Volume 34 | Issue 3 Article 2

2023
Section: Chemistry

Enhanced Adsorption of Anionic Dyes using Sr-Doped ZnO Nanoparticles: Nonlinear Kinetics and Isotherm Studies

Mostafa H. Mohamed
Department of Chemistry, Faculty of Science, Al-Azhar University, Cairo 11884, Egypt

Taha M. Elmorsi
Department of Chemistry, Faculty of Science, Al-Azhar University, Cairo 11884, Egypt,
taha_elmorsi@azhar.edu.eg

H. M. Abdelbary
Department of Chemistry, Faculty of Science, Al-Azhar University, Cairo 11884, Egypt

How to Cite This Article

Mohamed, Mostafa H.; Elmorsi, Taha M.; and Abdelbary, H. M. (2023) "Enhanced Adsorption of Anionic Dyes using Sr-Doped ZnO Nanoparticles: Nonlinear Kinetics and Isotherm Studies," *Al-Azhar Bulletin of Science*: Vol. 34: Iss. 3, Article 2.
DOI: https://doi.org/10.58675/2636-3305.1654

ORIGINAL ARTICLE

Enhanced Adsorption of Anionic Dyes Using Sr-doped Zno Nanoparticles: Nonlinear Kinetics and Isotherm Studies

Mostafa Hassan Mohamed, Taha Mahmoud Elmorsi*, Hassan Mohamed Abdel Bary

Department of Chemistry, Faculty of Science, Al-Azhar University, Cairo, Egypt

Abstract

Using a co-precipitation process, sr-doped zinc oxide (ZnO) was prepared and demonstrated to be effective in the removal of anionic congo red (CR) dye, since its surface positive charge was increased to 17.3 mV. To investigate the surface morphology and physicochemical characteristics of Sr-doped ZnO, FTIR spectroscopy, scanning electron microscopy (SEM), elemental analysis, and point of zero charges (pHPZC) were employed. We conducted batch adsorption experiments to investigate the effects of contact time (180 min), pH (3.5−11), adsorbent dosage (0.5−3.0g L−1), and temperature (288−328 K). The kinetic study was modeled using several equations, including pseudo-first-order (PFO), pseudo-second-order (PSO), Elovich, and intraparticle diffusion (IPD). For the purpose of describing the adsorption isotherm, Langmuir, Freundlich, and Temkin models were used. A pseudo-second-order model suggests that the adsorption process is chemisorption, which is further confirmed by the Langmuir isotherm model. The maximum capacity (q_{max}) of Sr-doped ZnO for removing CR dye was 71.83 mg/g. At natural pH, the % removal rate of CR dye increased from 13 % for pure ZnO (p-ZnO) to 82 % for Sr-doped ZnO, where the change in pH significantly increased the removal rate from 7.7 % at pH 11−92.0 % at pH 3.5. The thermodynamic parameters measured at 288, 298, 318, and 328 K indicate that the CR dye adsorption occurs spontaneously and endothermically. A significant role is also played by electrostatic interactions in the adsorption of anionic CR dye onto the positive surface of Sr-doped ZnO. This research study highlights the increased surface positivity of Sr-doped ZnO achieved through Sr ion doping. This resulted in a strong attraction to anionic dye molecules like CR dye. These findings collectively contribute to advancing the understanding of material−dye interactions and have potential implications for various applications in wastewater treatment and environmental remediation.

Keywords: Co-precipitation, Electrostatic attraction, Nonlinear kinetic and isotherm models, Spontaneous adsorption, Sr-doped zinc oxide

1. Introduction

The growth of the population and the industrialization of the world have made the provision of clean water and sanitary facilities more important than ever before. There are significant impacts caused by human activity on our water resources, which have caused this issue to receive unprecedented attention [1]. The availability of fresh water is essential for our survival and has contributed significantly to the achievement of a wide range of development goals across various sectors and nations [2]. Annually, millions of people lack access to clean [3], sterile water and pass away from illnesses brought on by tainted water. Among the industries that use organic dyes, which are produced in millions of tons a year, are textiles, plastics, printing, and cosmetics [4−9]. Despite their non-biodegradability and chemical resistance, dye solutions present a formidable challenge when it comes to their removal from the environment [9]. This is primarily due to their tendency to seep into aquatic

Received 23 July 2023; revised 27 August 2023; accepted 3 September 2023.
Available online 25 October 2023

* Corresponding author at: Department of Chemistry, Faculty of Science, Al-Azhar University, Cairo 11884, Egypt.
E-mail address: taha_elmorsi@azhar.edu.eg (T.M. Elmorsi).

https://doi.org/10.58675/2636-3305.1654

ecosystems where they can persist for extended periods, ultimately threatening the survival and prosperity of various forms of life [8]. Even in minor quantities, these dyes can cause substantial damage to living organisms. For instance, exposure to these substances can lead to irritations in the eyes, skin, and digestive tract when inhaled [9]. Moreover, dye-polluted industrial wastewater is a significant concern, considering it frequently lacks effective treatment before its release into the environment. This untreated discharge can lead to reduced sunlight penetration in bodies of water, thereby impeding photosynthesis. This, in turn, degrades aquatic ecosystems by reducing the levels of dissolved oxygen within lakes and rivers [10], a crucial element for the survival of aquatic life. The impact of dye effluents is further underscored by their role in contributing to water pollution. These effluents, once in the water system, pose substantial health risks to a wide range of organisms, including aquatic life, plants, and even humans. The ingestion or absorption of dye-contaminated water has been linked to a host of health complications, such as allergies, skin diseases, and more alarmingly, various forms of cancer. As a result, the issue of dye pollution demands urgent attention and effective solution strategies [11,12]. Aside from that, some dyes, like Congo red (CR), have a high level of toxicity and linger in the environment, which causes unwanted biomagnification. Many dyes, including CR [13], unintentionally cause biomagnification as a result of their elevated levels of toxicities and environmental retention [14–17]. In this case, it is extremely important that these colors be removed from wastewater [18]. Several methods can be used to remove the dye, including catalytic oxidation, ion exchange, nanofiltration, electrodialysis, electrocoagulation, bioremediation, ozonation, the Fenton reaction, and adsorption [17,19–25]. One of the most important techniques for the removal of harmful pollutants is adsorption, due to its adaptability, simplicity, reuse potential, cheap cost, and environmental friendliness [26,27]. A major advantage of nanomaterials is their unique physical and chemical properties, which include a moderate synthesis temperature [28], a large surface area, high adsorption capacity, and reasonable recyclability. Some of the nano-adsorbents identified include charcoal, carbon dots, carbon nanotubes, zeolites, metal oxides, activated carbon, organic frameworks, and porous materials [28–32]. In many cases, these adsorbents do not meet the necessary standards for adsorption selectivity or capacity. To apply adsorption to real applications, it is necessary to investigate efficient adsorbents. For the removal of organic pollutants from wastewater, zinc oxide (ZnO) has been used in a variety of morphologies over the past few decades [33]. The antibacterial and antifungal properties of zinc oxide have been well-documented for a long time. However, zinc oxide has also been found to possess a number of other properties besides its relatively low cost, its high biocompatibility, its chemical stability, and its nontoxicity to human cells, which have also contributed to its popularity [34–37]. There are several methods available today for generating ZnO nanoparticles (NPs) with high surface areas, as well as physical and chemical characteristics, such as co-precipitation, hydrothermal, and ultrasonic [38,39]. ZnO NPs are used in a variety of applications, including sensors, biosensors, optoelectronics, transducers, cosmetic ingredients, drug carriers, and dental filling materials. Furthermore, it has been extensively used to treat wastewater effluents and contaminated water by sorption and degradation processes [40,41]. In addition, ZnO can be doped with foreign metals including magnesium, aluminum, and strontium [38,40] in order to enhance its properties. However, the doping process is affected by a number of factors including the ionic radius, the invariance of the lattice constant, and the solubility of the foreign metal in ZnO. Due to their enhanced properties, doped ZnO NPs are widely used in sorption processes [42]. In this study, nanoparticles of p-ZnO and Sr-doped ZnO (6, 10, 15, and 20 wt. %) were evaluated as potential absorbents for the removal of CR dye from wastewater. CR dye adsorption by Sr-doped ZnO was higher than pure ZnO at various pH levels, with more than 92% of CR to be absorbed. We examined the adsorption kinetics and isotherms of Sr-doped ZnO NPs by adjusting pH, adsorbent dosage, contact time, and starting dye concentration.

2. Chemicals and synthesis procedures

Chemicals used in this study without further treatment zinc acetate dihydrate ($Zn(CH_3CO_2)_2.2H_2O$, (99.0 %) strontium chloride hexahydrate ($SrCl_2.6H_2O$), (99.9 %), and CR an anionic dye of disodium salt ($C_{32}H_{22}N_6Na_2O_6S_2$), (99.9 %) were obtained from LOBA Chemie Company, India (Fig. 1). NaOH, HNO_3 (68 %) and C_2H_5OH (80 %) were obtained from Oxford Laboratory Reagent Company.

2.1. Synthesis of pure ZnO and Sr-doped ZnO nanoparticles (NPs)

In this study, NPs pure ZnO (p-ZnO) and Sr-doped ZnO nanoparticles (Sr-doped ZnO) with

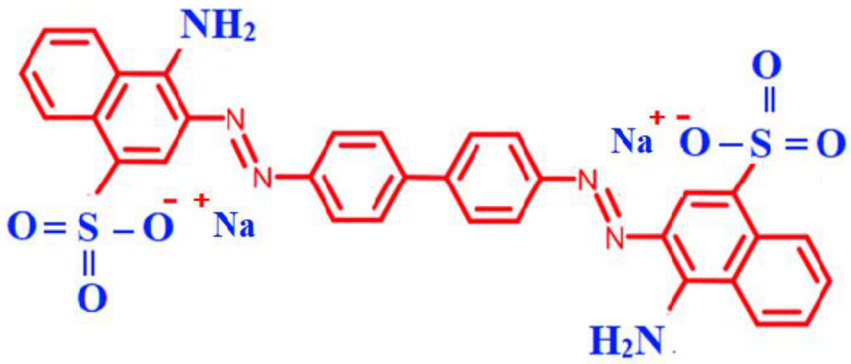

Fig. 1. Chemical structure of congo red (1-naphthalenesulfonic acid-3,3′- (4,4′-biphenylene bis (azo)) bis (4-amino-)).

different % wt. were synthesized by co-precipitation method.

2.1.1. Synthesis of P–ZnO NPs

To prepare P–ZnO NPs a 2 : 1 ratio of NaOH: Zn^{+2}) ions was used ([43]. An aqueous solution of 12 mmol NaOH (20 ml) was added dropwise to 6 mmol $(CH_3COO)_2$ $Zn.2H_2O$ then diluted to 20 ml of distilled water (DW) and kept on the magnetic stirrer at 120 rpm. A white precipitate of P–ZnO was produced and dried at 70 °C for 15 h. Diluted aqueous solution of ethyl alcohol (70 : 30%) was used to clean up the former white precipitate.

2.1.2. Production of Sr-doped ZnO

Production and doping process of Sr-doped ZnO conducted (similar to the synthesis of P–ZnO) in one step by adding Sr^2 ions at four different percentages (6, 10, 15, and 20 wt.%). The procedure involved adding 20 ml of 12 mmol NaOH aqueous solution dropwise to 20 ml of 6 mmol of $(CH_3COO)_2Zn.2H_2O$ and the specified % of $SrCl_2$ with continuous stirring at 120 rpm. Precipitates of Sr-doped ZnO were dried and washed in a similar manner to those of P–ZnO. The adsorption efficiency of Sr-doped ZnO to remove CR dye from aqueous solution was evaluated in comparison to the efficiency of P–ZnO.

2.2. Analyzing the synthetized adsorbents

To characterize the samples of P–ZnO and Sr-doped ZnO (6, 10, 15, and 20 wt. %), a variety of techniques were used. Panalytical-Netherland X'Pert PRO was used to perform radiography diffraction (XRD) of the prepared samples at room temperature. A scan mode measurement was conducted using Cu-Kα radiation (λ = 0.1542 nm) from 30 to 70. Functional groups and structural properties were analyzed with an FTIR spectrometer (Thermo Fisher Scientific, Carlsbad, USA). Using scanning electron microscopy (SEM), samples were characterized for size, morphology, and structures. Morphology and elemental analysis were performed using a scanning electron equipped with an energy-dispersive radiography (EDX). The Zeta potential of synthesized samples was determined by a Litesizer 500 equipped with a 40 mW 658 nm laser and Omega Cuvette cells. The electrophoretic motion of particles is used to compute Zeta potential [43].

2.2.1. Measuring point of zero charge

The charge of the surface of Sr-doped ZnO was described by measuring the point of zero charge (PZC). A specific amount of the Sr-doped ZnO (0.1 g) was added to 20 ml of 0.1 M KCl solutions at known initial pH (pH_i) values (3, 5, 7, 8, 9, 10, and 11). The suspensions were stirred at room temperature for 24 h to reach equilibrium then filtered and used to measure the final pH values (pH_f). The resulting curve of the plot of pH_i and ΔpH ($=pH_f - pH_i$) used to determine the PZC as the point of the intersection at which the ΔpH = zero for P–ZnO and the Sr-doped ZnO.

2.2.2. Adsorption experiments

Dissolving one gram of CR dye in one liter of distilled water provided a 100 ppm stock solution of CR dye. During 10 h at 120 rpm, the mixture was constantly stirred to ensure homogeneity. Several calibration curves were prepared using the stock solution, and adsorption experiments were conducted using both P–ZnO and Sr-doped ZnO with diluted stock solutions. To a known volume of CR dye (V_L) in stirred glassware (at 120 rpmmass of adsorbent powder (m) was added. In order to determine the absorbance of the remaining CR dye concentration, all solutions were centrifuged to separate the adsorbent powder. Accordingly, the

effects of the initial concentration of CR, the dosage of adsorbent powder, pH, and temperature were studied on the adsorption process of dye.

2.3. Analytical procedures

A Jenway UV–visible spectrophotometer was used to measure the initial concentration (C_0), the concentration at any time (C_t) and the concentration at equilibrium (C_e) for CR dye during the adsorption experiments. The value of these different concentrations based on the calibration curve were used to determine the adsorption capacity, or the quantity of CR adsorbed onto P–ZnO and Sr-doped ZnO at any given time (q_t) and at equilibrium (q_e) along wit the % removal as shown in Eqs. (1)–(3), respectively [44].

$$= \frac{(C_0 - C_t)\, x\, V}{m} \tag{1}$$

$$= \frac{(C_0 - C_e)\, x\, V}{m} \tag{2}$$

Also, % removal of CR was calculated [45] according to Eq. (3)

$$\%\ Removal = \frac{C_0 - C_t}{C_0}\, x\, 100 \tag{3}$$

2.4. Kinetics of the adsorption

The kinetics data of the CR dye adsorption onto P–ZnO and Sr-doped ZnO was modeled using nonlinear kinetic models of pseudo-first-order (PFO), pseudo-second-order (PSO), Elovich kinetic equations, and the linear form of intraparticle diffusion (IPD)equation [46,47] as shown in Eq. (4)–(7) respectively.

$$q_t = q_e\left(1 - e^{-k_1 t}\right) \tag{4}$$

$$q_t = \frac{k_2 q_e^2 t}{1 + k_2 q_e t} \tag{5}$$

$$q_t = \frac{1}{\beta}\ln\left(1 + \alpha\beta t\right) \tag{6}$$

$$q_t = K_{id}\sqrt{t} + C \tag{7}$$

According to these equations, k_1, and k_2, indicate the rate constants of PFO and PSO, respectively; k_{id}, and C, represent the IPD rate constant and intercept (indicating the thickness of the boundary layer); α and β refer to the initial rate of uptake and surface coverage.

2.5. Effect of temperature

Adsorption experiments were conducted to determine the effect of temperature on the adsorption of CR dye onto Sr-doped ZnO (15wt.%). Four different temperatures (288, 298, 318, and 328 K, respectively) at pH 3.5 were specified to evaluate the thermodynamic parameters including changes in enthalpy (ΔH), entropy (ΔS), and free energy (ΔG) [48].

2.6. Adsorption isotherm

As part of this study, three nonlinear isotherm models, Langmuir, Freundlich, and Temkin (Eqs. (8)–(10)), were used to evaluate the adsorption isotherm of CR dye (50–250 mg/l) onto Sr-doped ZnO at room temperature and pH 3.5. The equations yield K_L, K_f, q_{max}, n, A_T, and b_T which are the Langmuir and Freundlich constants, respectively, the maximum theoretical adsorption capacity, Temkin binding constant and Temkin constant related to adsorbent–adsorbate interactions. Eq. (11) shows that R is the universal gas constant, T is the temperature (K), and B is the heat of the sorption constant [44].

$$q_e = K_f\, C^{1/n} \tag{8}$$

$$q_e = q_{max} K_L \left(\frac{C_e}{1 + K_L C_e}\right) \tag{9}$$

$$q_e = \frac{RT}{b_T}\left(\ln C_e + \ln A_T\right) \tag{10}$$

$$B = \frac{RT}{b_T} \tag{11}$$

3. Findings and discussion

3.1. Analyses of P–ZnO and Sr-doped ZnO (6, 10, 15 and 20 wt. %)

3.1.1. The X-ray diffraction (XRD) method

An XRD analysis was performed on the prepared adsorbents (P–ZnO and Sr-doped ZnO (6, 10, 15, and 20 wt. %)) to assess their purity and crystallinity. Fig. 2 shows the crystalline phase and purity of standard ZnO (JCPDS No. 36–1451), P–ZnO and Sr-doped ZnO (6, 10, 15, and 20 wt. %) nanoparticles. It is clear that this pattern is in high agreement with the phase of standard ZnO (JCPDS Card No. 36–1451), which is hexagonal wurtzite polycrystalline structure space group: P63mc (186) with

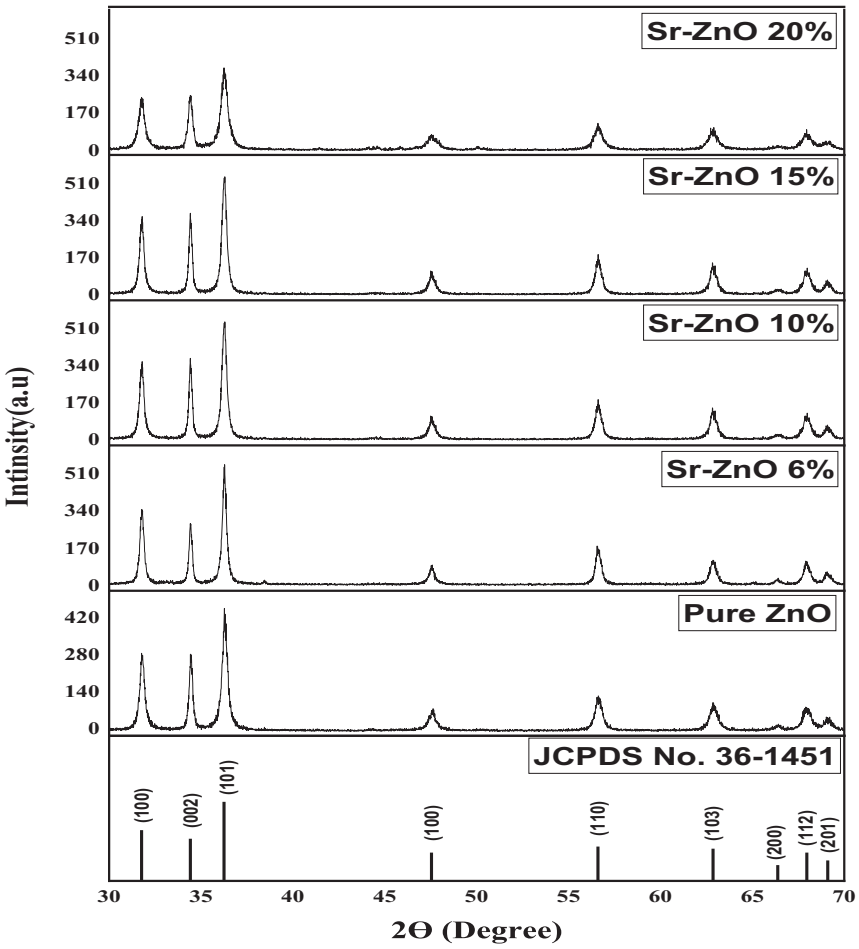

Fig. 2. Radiography diffraction pattern of standard ZnO (JCPDS No. 36–1451), pure ZnO (P–ZnO) and Sr-doped ZnO (6, 10, 15, and 20 wt. %).

lattice planes (hkl) as: (100), (002), (101), (102), (110), (103), (200), (112), and (201), respectively.

Table 1 demonstrates the lattice parameters (a, b, and c), lattice volume, and crystallite size of P–ZnO and Sr-doped ZnO as determined by XRD data. Lattice parameters (a and c), which were calculated using Eq. (12), were used to evaluate the influence of % wt. of Sr ions on crystal structure:

$$\frac{1}{D_{hkl}} = \frac{4}{3}\left(\frac{h^2 + hk + k^2}{a^2}\right) + \frac{l^2}{c^2} \quad (12)$$

The planes (100) and (002) were used to determine the lattice parameters *a* and *c*, respectively.

As a result of the increase in lattice parameters and the absence of any unreacted substances, it was concluded that strontium ions (Sr^{2+}) ions had been

Table 1. The lattice parameters (a, b, and c), lattice volume, and crystallite size of P–ZnO and Sr-doped ZnO (6, 10, 15, and 20 wt. %) as determined by radiography diffraction data.

% doping	Miller indices	d spacing (A)	a (A)	b (A)	c (A)	2Θ (Degree)	Lattice Volume (A)^3	Crystal size (nm)
P–ZnO	(100)	2.8096	3.2442	5.2047	1.6043	47.4383	3.2442	18.12
	(200)	2.6023						
Sr-doped ZnO 6 %	(100)	2.8117	3.2467	5.2068	1.6037	47.5114	3.2467	19.36
	(200)	2.6034						
Sr-doped ZnO 10 %	(100)	2.8129	3.2480	5.2126	1.6048	47.6216	3.2480	22.14
	(200)	2.6063						
Sr-doped ZnO 15 %	(100)	2.8152	3.2507	5.2143	1.6040	47.7164	3.2507	24.84
	(200)	2.6021						
Sr-doped ZnO 20 %	(100)	2.8129	3.2480	5.2126	1.6048	47.6216	3.2480	27.45
	(200)	2.6063						

successfully doped into ZnO. It also confirmed the high purity of synthesized P–ZnO and Sr-doped ZnO (6, 10, 15, and 20 wt. %) nanoparticles [49]. Additionally, the XRD pattern showed peaks that were sharp and strong, which indicates that the Dkhl crystals are highly crystallized [50].

It was noted that increasing Sr content from 6 to 20 % in Sr-doped ZnO results in a decrease in the angle shift of diffraction peaks as well as an increase in the crystal lattice expansion. According to Fig. 3, the diffraction peaks of the Sr-doped ZnO (6, 10, 15, and 20 wt. %) were shifted to lower angles than those for P–ZnO. This may be due to the larger ionic radius of Sr^{2+} (0.113 nm) compared with Zn^{2+} (0.074 nm) [51], which will result in the expansion of the crystal lattice and in a lower angle shift in the diffraction peak.

To determine crystallite size (D_{hkl}), Debye–Scherrer (Eq. (13)) was applied as follows:

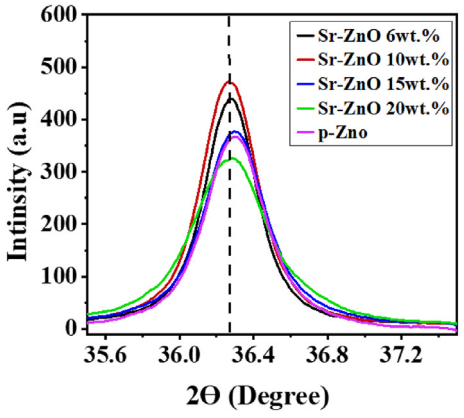

Fig. 3. A shift of the diffraction peaks of Sr-doped ZnO (6, 10, 15, and 20 wt. %) to lower angles than P–ZnO.

$$D_{hkl} = \frac{K\lambda}{\beta_{hkl}\cos\theta_{hkl}} \quad (13)$$

Assume that K represents a constant of 0.94, λ represents an radiography wavelength, θ_{hkl} represents a Bragg angle, and β_{hkl} represents the full width at half maximum of the diffraction peak. Due to the large ionic radius of Sr^{2+} ions, the crystallite size of Sr-doped ZnO increases to 27.5 nm compared with 18.2 nm for P–ZnO.

3.1.2. FT-IR spectroscopic analysis

A diagnostic peak of ZnO was detected in the fourier-transform infrared spectroscopy (FTIR) spectrum (Fig. 4) in the range of 400–600 cm^{-1}. The Sr-doped ZnO (6, 10, 15, and 20 wt. %) are observed at 459, 456.74, 461.88, and 455.13 cm^{-1}, respectively. Furthermore, the peak at 850-870 cm^{-1} is indicative of SrO, along with a weak peak at 1790 cm^{-1} caused by asymmetric vibrations in $SrCO_3$. Water molecules are physiosorbed on Sr-doped ZnO adsorbents, as evidenced by a broad band at 2900–3700 cm^{-1} caused by the stretching mode of the OH groups.

3.2. Morphology and elemental analysis

A microscopy image of the synthesized adsorbents (P–ZnO and Sr-doped ZnO (6, 10, 15, and 20 wt. %)) has been shown in Fig. 5a-e. In these images, surface aggregation of the adsorbent nanoparticles is clearly visible. This may be due to an increase in the surface area to volume ratio as well as an increase in surface energy. The increased surface energy associated with aggregation can enhance the interaction between Sr-doped ZnO (6, 10, 15, and 20 wt. %) and CR dye. A strong

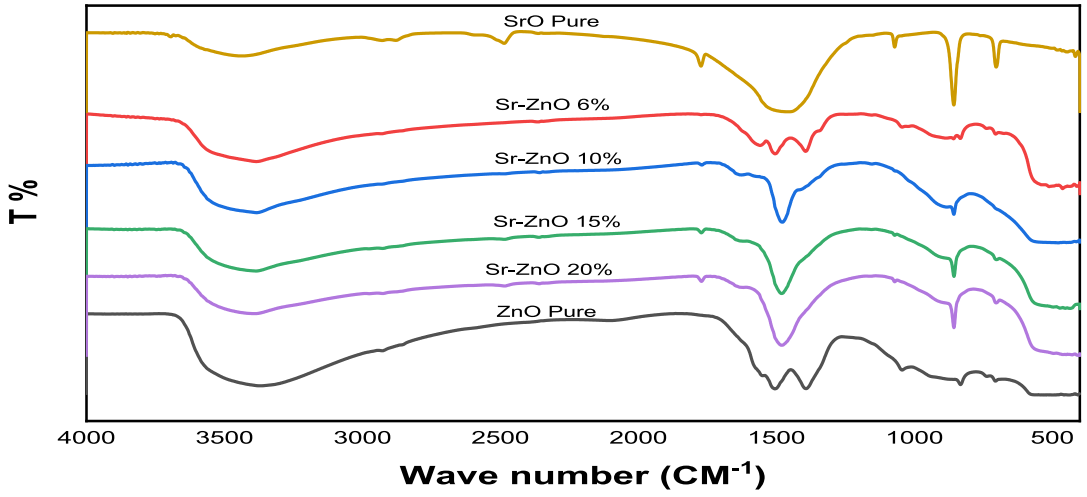

Fig. 4. FTIR Spectra for Pure SrO, pure ZnO and Sr-doped ZnO (6, 10, 15, and 20 wt. %).

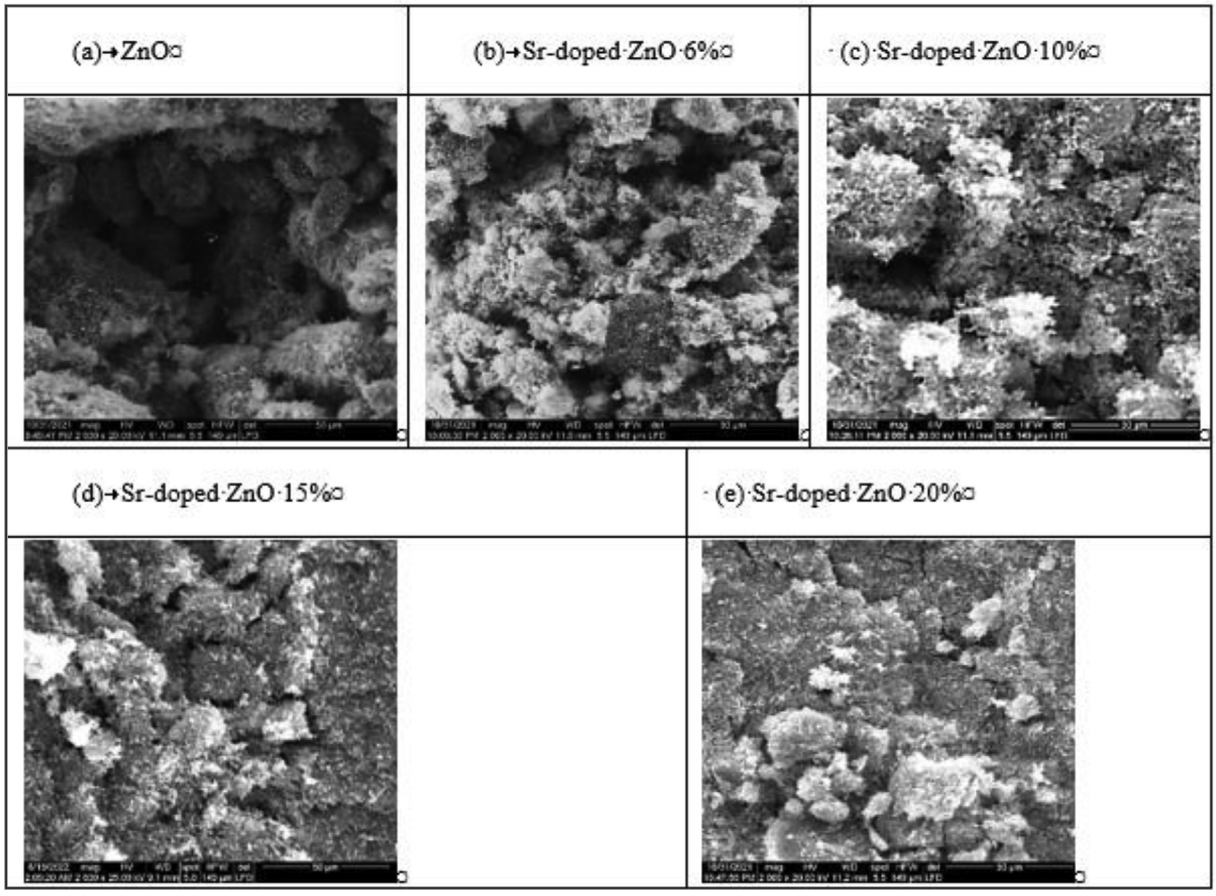

Fig. 5. SEM images for (a) Pure ZnO (b) Sr-doped ZnO 6 % (c) Sr-doped ZnO 10 % (d) Sr-doped ZnO 15 % (e) Sr-doped ZnO 20 wt.%.

electrostatic interaction between the negative anionic molecules of CR dye and the positive surface of the adsorbent may result in greater adsorption capacities. The accumulation of Sr ions during the doping process prevents the dispersal of Sr-doped ZnO, potentially resulting in larger aggregates. The specific effect of Sr-doping on adsorption performance may, however, vary depending on the interaction between the adsorbent and the adsorbate. In this study, it was demonstrated that where the presence of Sr ions enhanced surface positivity, anionic CR dye molecules would attract more readily. As a consequence, Sr-doped ZnO (15 wt%) showed a dramatic increase in CR dye removal when compared with P−ZnO, as will be discussed in more detail in the next section.

In a quantitative EDS analysis of P−ZnO and Sr-doped ZnO (6, 10, 15, and 20 wt. %), Zn, and O were detected. On the basis of the determined amount of O, the weight percentage of ZnO decreases with an increase in Sr-doping weight percentage, without the presence of impurities. This indicates that the doping process was successful (Table 2).

3.2.1. Point of zero charge (pzc) and zeta potential

ZP [27] indicates the variation in surface charges between the colloidal suspension of the nanoparticles and the solution and is used as a measure

Table 2. Mass % and atomic % of main surface elements in P−ZnO and Sr-doped ZnO (6, 10, 15 and 20 wt. %) with different doping percent samples as calculated from EDS spectrum.

Element	P−ZnO		Sr-doped ZnO (6 wt.%)		Sr-doped ZnO (10 wt.%)		Sr-doped ZnO (15 wt.%)		Sr-doped ZnO (20 wt.%)	
	Mass %	Atomic %	Mass %	Atomic %	Mass %	Atomic %	Mass %	Atomic %	Mass %	Atomic %
O	21.02	52.11	19.86	50.6	19.46	49.8	19.8	50.22	20.13	51.57
Sr	0	0	5.61	2.56	9.71	4.57	14.61	6.7	19.34	9.9
Zn	78.93	47.82	74.5	46.82	70.81	45.5	65.43	42.89	60.44	38.45
Total	99.95	99.93	99.97	99.98	99.98	99.87	99.84	99.81	99.91	99.92

of stability [52]. As a result of the doping process, the ZP value of Sr-doped ZnO 15 wt.% increased to 17.3 mV as compared with 3.5 mV for P–ZnO. Accordingly, Sr-doped ZnO is moderately suspended in the solution and possesses positive charges, which may facilitate the adsorption of anionic CR dye via electrostatic interaction, depending on the solution pH. Previously, it was reported that the doping process increased CO_2 adsorption [53]. In addition, we determined the PZC using the pH drift method to be 7.6 in the case of Sr-doped ZnO 15 wt.%.

3.3. Effect of Sr-doped ZnO on CR dye adsorption

In order to investigate the effects of Sr-doped ZnO on CR dye adsorption, screening experiments were conducted using both P–ZnO and Sr-doped ZnO (6, 10, 15, and 20 wt. %) at room temperature and natural pH for 60 min. As shown in Fig. 6 P–ZnO was less effective, removing only 13 %, while the % removal increased dramatically to 82 % in the presence of Sr-doped ZnO (15 wt.%). In addition, the % removal increased from 72 % to 82 % in 60 min when Sr content was raised from 6 to 15 wt.% in ZnO. However, increasing the amount of Sr to 20 wt.% did not result in a significant increase in removal percentage. Therefore, in the subsequent experiments, the Sr-doped ZnO (15 wt.%) adsorbent was the most effective. Although doping with Sr ions produces positive charges on the surfaces, these charges facilitate the removal of anionic CR dyes by electrostatic attraction [54]. In addition, it may change the surface electronegativity [55] resulting in a stronger electrostatic interaction with dyes having an opposite charge.

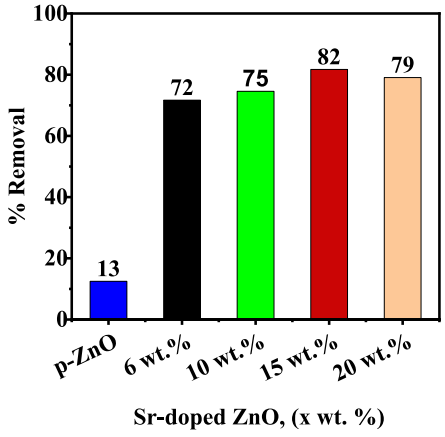

Fig. 6. Effect of Sr doping wt.% on the adsorption of CR onto P–ZnO and Sr-doped ZnO (6, 10, 15, and 20 wt. %), at natural pH, room temperature, ($[CR]_o$ = 50 mg L^{-1}, time = 60 min, adsorbent dosage = 1.5 g L^{-1}).

3.4. Effect of adsorbent dosage

Sr-doped ZnO (15 wt.%) doses (0.5–3 gL^{-1}) were tested at room temperature and at an optimal pH value to determine their effects on the adsorption of CR dye ($[CR]o = 50$ mg L^{-1}). Fig. 7 shows that the % removal of CR dye in the presence of Sr-doped ZnO (15 wt. %) was rapid and proportional to the amount of adsorbent used. Approximately 45 % of CR dye was removed from the solution when 0.5 g L^{-1} of adsorbent was added to the solution. In another CR dye solution, more adsorbents were added under identical conditions. An increase in the adsorbent dose to 1.5 g L^{-1} resulted in a significant increase in the % removal to 85 %. It is possible to attribute the increase in adsorbent surface area and the availability of additional adsorption sites to the increasing efficacy of CR removal as the adsorbent dose is increased [56]. A slight improvement in the disappearance was observed by increasing the quantity of Sr-doped ZnO (15 wt.%) in the solution from 1.5 to 3 g L^{-1}. The presence of a large amount of adsorbent can result in the accumulation of grains on the adsorbent surface, thereby reducing the number of exposed sites and surface area, and thereby decreasing the removal rate of CR dye [31]. For the following tests, 1.5 g L^{-1} of Sr-doped ZnO (15 wt.%) was determined to be the optimal dose.

3.5. Effect of pH

An adsorption experiment with CR dye (50 mg/L) was conducted within a pH range of 3.5–11 in order to investigate the effects of pH on adsorption. Upon decreasing the pH value from 11 to 3.5, the concentration of dye in the solution dramatically

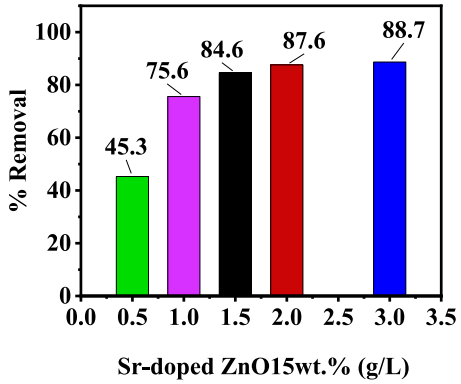

Fig. 7. The effect of Sr-doped ZnO (15 wt. %) dose (g L^{-1}) on the % removal of congo red dye at room temperature and pH 3.5.

increased from 7.7 % at pH 11–92.0 % at pH 3.5 as shown in Fig. 8. This result can be explained by the pHPZC of Sr-doped ZnO (15 wt.%) (as an indication of active surface groups) and the polarity (ionic character) of CR dye, which is dependent on solution pH [57]. The pHPZC of Sr-doped ZnO (15 wt.%) was found to be around pH 7.6. The surface of Sr-doped ZnO becomes negatively charged at pH 11 (pH > pHPZC), resulting in significant electrostatic repulsion with the anionic CR dye. A second reason for the minimal adsorption is that OH-ions present in the basic solution compete with anionic CR dyes for adsorption sites. A positively charged surface of Sr-doped ZnO is formed at pH 3 (pH greater than pHpzc), which allows an anionic CR dye to be adsorbed due to electrostatic interactions. A similar result was obtained when CR dye was adsorbable on pine bark [58].

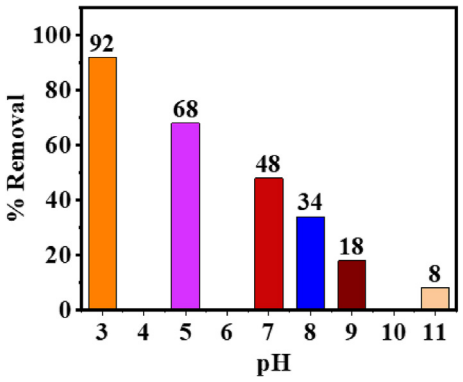

Fig. 8. Effect of pH on % removal of congo red by Sr-doped ZnO (15 wt. %), ([congo red]0 = 50 mg L^{-1}, time = 90 min, Sr-doped ZnO (15 wt.%) dosage = 1.5 g L^{-1}), at room temperature.

3.6. Effect of contact time and adsorption kinetics of CR dye

The effect of contact time on CR dye adsorption was investigated using various concentrations of CR dye (50, 100, and 200 mg L^{-1}). It was found that there were two stages involved in the removal of the three initial concentrations by Sr-doped ZnO (15 wt.%) and equilibrium was achieved in 60 min as shown in Fig. 9a. In the case of 50 mg/l CR dye, ~73 % had been removed within 15 min. As the contact time increased, the percentage of removal increased to 87 % and equilibrium was reached after

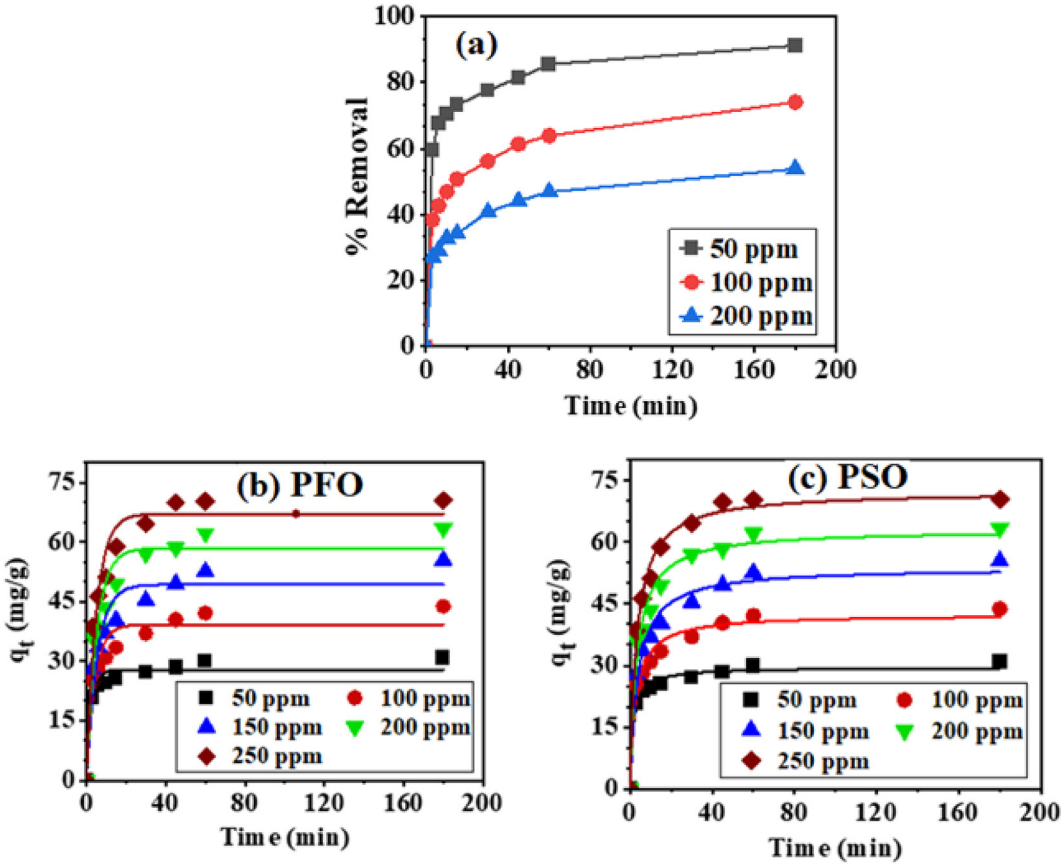

Fig. 9. Effect of contact time on the % removal of congo red dye (a), nonlinear pseudo first-order (b) and pseudo second-order model (c) for the adsorption of congo red dye onto Sr-doped ZnO at pH 3 and at room temperature.

approximately 60 min. However, upon an increase in contact time by threefold, the % of removal improved only slightly to 91.1 %. It is indicated that contact time has a significant effect on the adsorption process. Other concentrations of 100–200 mg L^{-1} showed a similar trend [59]. Further, it will be valuable to investigate the kinetics of CR dye adsorption in order to gain a better understanding of the mechanism of adsorption. In order to investigate the kinetics of the process, three nonlinear models were used including PFO, PSO, and Elovich equations (Eqs. (4)–(6)). Linear regression may adversely affect kinetic data due to the conversion of nonlinear forms to linear forms [44]. Two statistical error analyses were performed using Origin Software, including a Reduced χ^2 (Red Chi-Square) and a Coefficient of Determination (R^2). According to Fig. 9b-c and the calculated parameters in Table 3, PSO obtained a high R^2. value (0.960–0.992) and a low Red χ^2value. The Red χ^2value for all initial concentrations under investigation (50–250 mg L^{-1}) ranged between 0.76 and 15.60. Additionally, the calculated values of qe (Table 3) are in satisfactory agreement with the experimental results. The kinetic adsorption of CR dye is described by the PSO model. Based on the results, it can be concluded that the anionic CR dye is chemisorbed onto the positively charged Sr-doped ZnO via electrostatic interactions. Previously, similar results were reported [60]. To further investigate the kinetic study, experimental data were examined with both Elovich and IPD models (Eqs. (6) and (7)) as shown in Fig. 10 a and Table 4. The results show that the Elovich equation is suitable to describe CR dye adsorption based on high R^2 values and low Red. Ch-Sqr values. Also, the desorption constant values obtained from the Elovich model (β) are small (0.12–0.4 mgg^{-1}) indicating an irreversible CR dye adsorption process. Using the IPD equation, the experimental data was further analyzed, and the results are illustrated in Fig. 10b. Experimental curves did not pass the origin and showed more than one step. As shown in Table 4, the IPD rate constant (K_{id}) is calculated from the slope of each linear stage. Each curve displayed a higher diffusion rate at its first stage and a slower diffusion rate at its second stage. The results of this study suggest that IPD is not the only process involved. In contrast, there are multiple mechanisms involved in the diffusion of CR dye into

Table 3. Nonlinear parameters of pseudo-first-order and pseudo-second-order for the adsorption of congo red dye onto Sr-doped ZnO at pH 3 and at room temperature.

Nonlinear Pseudo First-Order						Nonlinear Pseudo Second-Order			
[MB] ppm	$q_{e,exp}$ (mg g^{-1})	$q_{e,cal}$ (mg g^{-1})	k_1 (g min^{-1})	R^2	Red. Chi-Sqr	$q_{e.(cal)}$ (mg g^{-1})	k_2 (g/(mg·min)	R^2	Red. Chi-Sqr
50	30.84	27.52 ± 0.77	0.407 ± 0.07	0.965	3.42	29.13 ± 0.478	0.025 ± 0.004	0.992	0.76
100	43.79	40.49 ± 2.35	0.207 ± 0.05	0.889	24.93	44.30 ± 1.98	0.007 ± 0.002	0.960	9.9
150	55.42	49.88 ± 2.70	0.178 ± 0.04	0.908	31.20	54.81 ± 2.13	0.005 ± 0.001		10.60
200	63.43	57.16 ± 3.09	0.12 ± 0.05	0.902	42.52	62.03 ± 2.44	0.005 ± 0.001	0.970	
250	70.44	63.14 ± 2.57	0.227 ± 0.043	0.941	30.96	68.28 ± 1.59	0.005 ± 7.7E-4	0.970	15.16

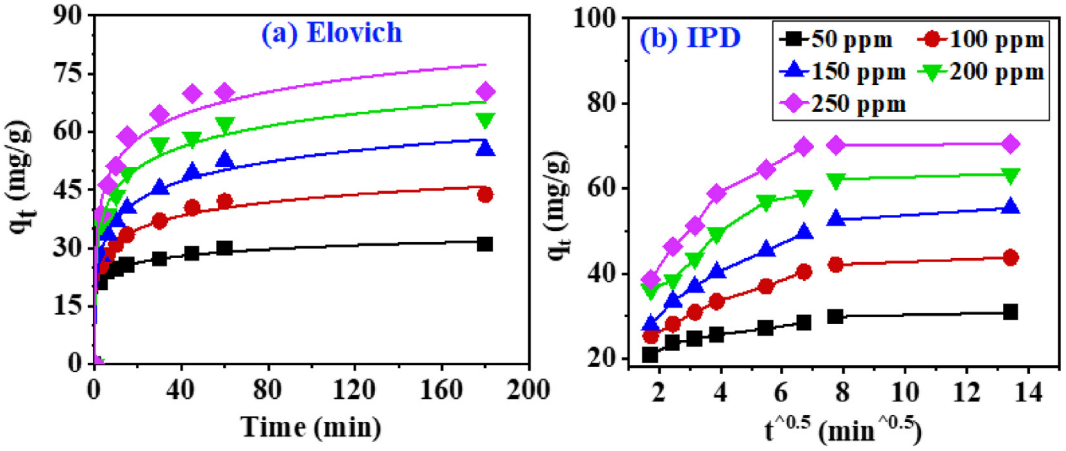

Fig. 10. The nonlinear curves of Elovich model (a) and the intra-particle diffusion model (b) for the ad-sorption of congo red dye onto Sr-doped ZnO (15 wt. %) at pH 3.5 and at room temperature.

Table 4. Nonlinear parameters of Elovich and intra-particle diffusion model for the adsorption of congo red dye onto Sr-doped ZnO (15 wt. 15 %) at pH 7.5 and at room temperature.

Nonlinear Elovich Model						Intra-particle diffusion (IPD)			
[CR] ppm	$q_{e,exp}$ (mg g^{-1})	β (g mg^{-1})	α (mg/g/min)	R^2	Red. Chi-Sqr	K_p (mg/g/ $tmin^{0.5}$)	C	R^2	RSS
50	30.84	0.40	4769.1	0.997	0.32	1.37 ± 0.196	19.69 ± 0.834	0.925	2.7
100	43.79	0.20	266.5	0.993	1.47	2.95 ± 0.173	21.00 ± 0.740	0.986	2.1
150	55.42	0.14	128.9	0.993	2.23	4.11 ± 0.353	22.87 ± 1.50	0.971	8.8
200	63.43	0.13	259.9	0.984	7.35	4.87 ± 0.512	28.22 ± 2.18	0.958	18.6
250	70.44	0.12	355.6	0.974	15.00	6.08 ± 0.670	31.18 ± 2.85	0.954	31.8

Sr-doped ZnO. Among the three models, CR dye adsorption was more closely related to PSO than to Elovich and to IPD.

3.7. Effect of initial concentration and adsorption isotherm of CR dye

We determined the effects of starting [CR] dye (50–250 mg L^{-1}) at pH 3.5 using 1.5 gL^{-1} Sr-doped ZnO (15 wt.%), at room temperature for 180 min. The results indicated that the equilibrium adsorption capacity (qe) of CR dye increases from 29.98 to 69.83 mgg^{-1} with the increase in the initial [CR] from 50 to 250 mg L^{-1} as shown in Fig. 11a. At higher dye concentrations the driving force may exceed the mass transfer resistance of CR dye ions [61,62] allowing an increase in the qe values. Additionally, increasing the initial concentration of CR dye from 50 to 250 mg L^{-1} may contribute to the saturation of all active sites with CR dye ions. It is accomplished by reaching an equilibrium state that facilitates the calculation of the theoretical maximum adsorption capacity of CR dye (qmax) using adsorption isotherm models. The

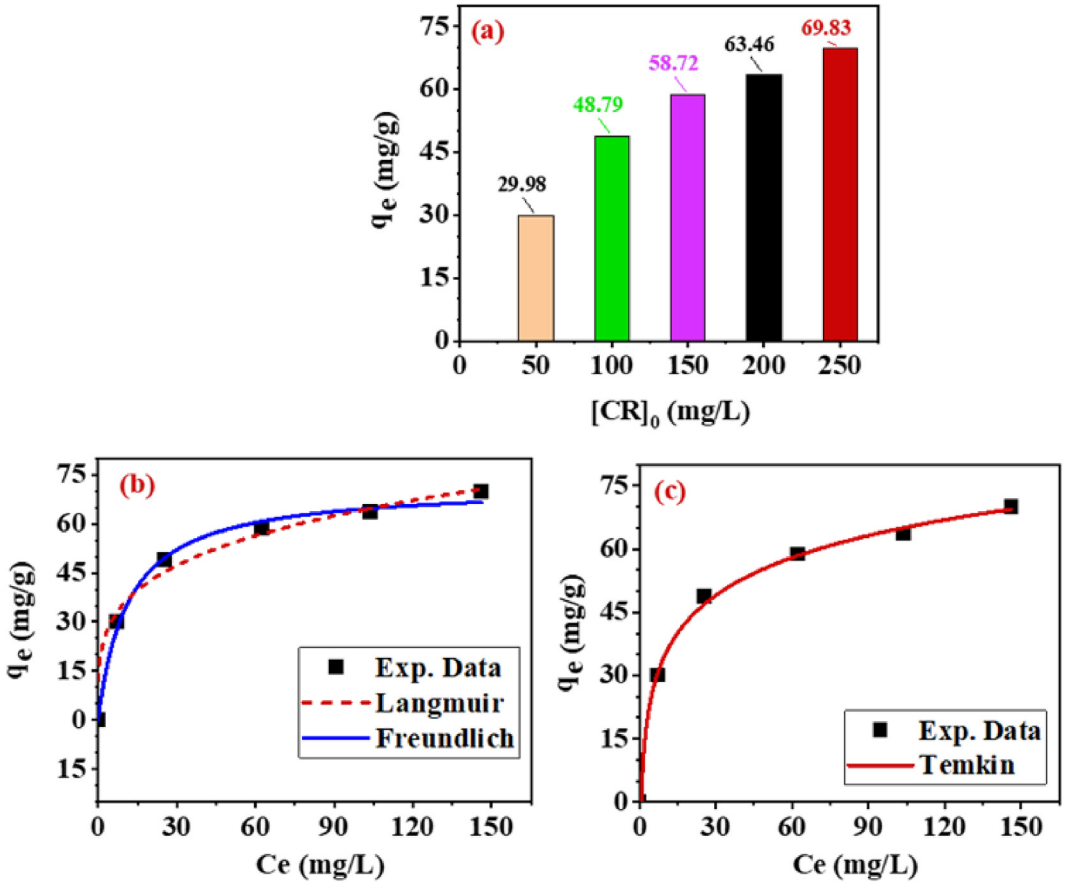

Fig. 11. Effect of initial concentration (50–250 mg L^{-1}) of congo red dye (a) and Langmuir and Freundlich nonlinear forms of adsorption isotherm (b) and Temkin model (c) for the adsorption of congo red onto Sr-doped ZnO at pH 3.5 and at room temperature.

experimental data were analyzed using different nonlinear isotherm models, such as Langmuir, Freundlich, and Temkin equations (Eqs.(10)–(12)). It was done in order to better understand the type of adsorption (monolayer or multilayer) as well as the interaction between the CR dye and the Sr-doped ZnO. The plot of qe versus Ce (Fig. 11b), together with the calculated parameters and the statistical error functions in Table 5, illustrates the applicability of Langmuir and Freundlich. A high value of R2 (0.994) and a low value of Red Chi-Sqr (4.85) indicated that the adsorption of CR dye onto Sr-doped ZnO followed the Langmuir isotherm model more closely than Freundlich. This study indicates that the CR dye adsorbed as a monolayer onto a homogeneous surface of Sr-doped ZnO (15 wt.%). The value of q_{max} was calculated as 71.83 ± 2.03 mgg^{-1}.

On the basis of the high value of R^2 (0.991) and low value of Red χ^2(1.77), the Temkin model was applicable to describe the adsorption data of CR dye. As a result, the isotherm studies of CR dye on Sr-doped ZnO followed the order Langmuir greater than Temkin greater than Freundlich. It has been reported that the adsorption of CR dye onto different adsorbents follows a similar pattern [63].

3.7.1. Comparison of the maximum capacity (q_{max}) of Sr-doped ZnO for removal of CR dye

The results in Table 6 indicated that the synthesized Sr-doped ZnO nanoparticles outperform many of the previously reported CR adsorbents. This finding is of particular significance as it highlights the practical applicability and potential advantages of using Sr-doped ZnO for CR dye removal.

3.7.2. Effect of temperature

This study examines the effects of temperature on CR dye adsorption on Sr-doped ZnO to determine the thermodynamic parameters of adsorption, including changes in enthalpy (ΔH°), entropy (ΔS°), and free energy (ΔG°) at 288, 298, 318, and 328K. We used the Van't Hoff isochoric (Eq. (14)) to determine the values of ΔH and ΔS. In addition, Eq (15) was used to determine the value of ΔG [64].

$$\ln K_C = \frac{\Delta S^\circ}{R} - \frac{\Delta^\circ}{R}\cdot\frac{1}{T} \tag{14}$$

$$\Delta G^\circ = -RT\ln K_C \tag{15}$$

$$K_C = \frac{C_i - C_e}{C_e} \tag{16}$$

Table 5. Nonlinear parameters and function errors of Langmuir, Freundlich and Temkin models for the adsorption of congo red dye onto Sr-doped ZnO (15 wt.%) at pH 3.5 and at room temperature.

	Langmuir Constants				Freundlich Constants				Temkin Constants				Red
	q_m (mg g^{-1})	K_L (L mg^{-1})	R^2	Red. Chi-Sqr	K_F (L mg^{-1})	n	R^2	Red. Chi-Sqr	B	b_T [g mol^{-1}]	A_T [L g^{-1}]	R^2	Chi-Sqr
CR dye	71.83 ± 2.03	0.088 ± 0.012	0.994	4.85	19.99 ± 2.5	0.25 ± 0.029	0.972	9.08	12.91 ± 0.55	72.48	1.48	0.991	1.77

Table 6. Comparison of adsorption capacity of various congo red dye adsorbents compared with Sr-doped ZnO.

Adsorbent	q_{max} (mg/g)	References
Hierarchical CuO–ZnO/SiO_2 (CZS)	141.8	[48]
Mg-doped ZnO (NPs)	125	[39]
Chitosan/beta-cyclodextrin/nanometer zinc oxide (CS/β-CD/Nano-ZnO)	96.33	[63]
Polyaniline modified ZnO (PANI@ZnO)	69.82	[12]
Sr-doped ZnO (15 wt. %)	71.83	This study

Where R is the universal gas constant (8.314 J mol^{-1}), T is the absolute temperature (K) and K_C (dimensionless) is the standard thermodynamic equilibrium constant. Also, C_i and C_e are the initial and equilibrium concentration of CR dye in solution respectively. The values of ΔH° and ΔS° were calculated from the slope and intercept of the plot of ln K_C versus $\frac{1}{T}$ as shown in Fig. 12.

The values of the thermodynamic parameters are represented in Table 7. It was noted that the negative values of ΔG° decreased from 2045 to −3936 kJ mol^{-1} due to the increase in the temperature from 288 to 318 K. This finding indicated that CR dye adsorption onto Sr-dopped ZnO (15 wt.%) is spontaneous, physisorption, and becomes more favorable at higher temperatures [64]. Also, CR dye adsorption is endothermic and there is a gradual increase in the amount of randomness at the solid/solution interface. This result is confirmed by the positive values of both ΔH (16.08 kJ/mol) and ΔS

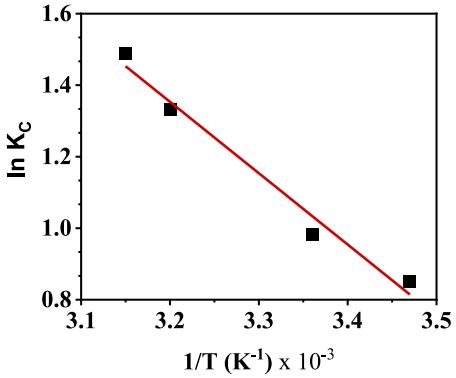

Fig. 12. Effect of temperature on the congo red adsorption onto Sr-doped ZnO (15 wt.%), ([congo red]0 = 100 mg L^{-1}, T = 288, 298, 308, and 318K, time = 180 min, pHi = 3.5, adsorbent dosage = 1.5 g L^{-1}).

Table 7. Thermodynamic parameters for adsorption of congo red dye onto Sr-doped ZnO (15 wt. %).

Temperature (K)	K_c	ΔG°	ΔH°	ΔS°
		KJ.mol^{-1}	KJ.mol^{-1}	KJ.mol^{-1}.K^{-1}
288	2.35	−2.045	16.08	0.064
298	2.67	−2.434		
308	3.79	−3.412		
318	4.43	−3.936		

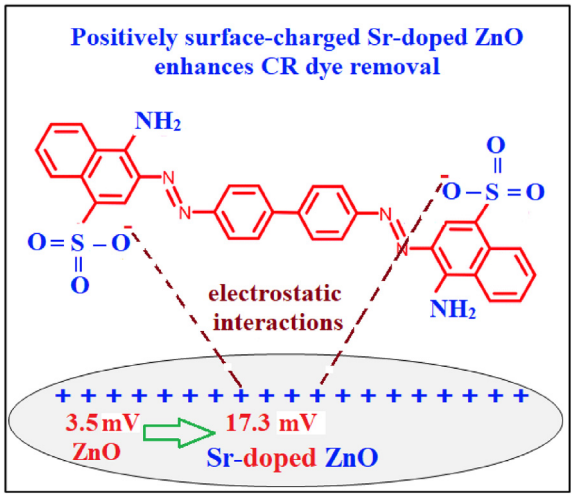

Fig. 13. Schematic representation of the adsorption mechanism of anionic congo red dye onto positively surface -charged Sr-doped ZnO through electrostatic interactions.

(0.07 kJ mol-1K-1). Previous studies were in good agreement with the current study [64].

3.8. Adsorption mechanism

The mechanism of CR dye adsorption onto Sr-doped ZnO is represented in Fig. 13. It was noted that the surface of Sr-doped ZnO was more positive than the surface of P–ZnO due to the increase of zeta potential from 3.5 to 17.3 mV. Also, CR dye ionizes in an aqueous solution and generates negative species as discussed previously. Furthermore, the adsorption process followed a PSO and showed an interaction between CR dye and the adsorbent. This was indicated by kinetic studies and Temkin adsorption isotherm. In conclusion, depending on the pH of the aqueous solution, electrostatic attraction may play a crucial role in the adsorption of anionic CR dye onto positively charged Sr-doped ZnO as shown in Fig. 13.

4. Conclusion

By using a co-precipitation method, Sr-doped ZnO was developed as an effective adsorbent for CR dyes. Sr-doped ZnO produced a highly effective adsorbent for an anionic CR dye with a positive zeta

potential of 17.3 mV as compared with 3.5 eV for P–ZnO. Four models were used to model the kinetics of the adsorption process: PFO, PSO, Elovich, and IPD. Freundlich, Langmuir, and Temkin models were used to investigate the adsorption isotherm. The PSO and Langmuir models provided a fundamental understanding of the formation of a chemisorption monolayer of CR dye on a homogeneous surface of Sr-doped ZnO. According to the Langmuir model, Sr-doped ZnO (15 wt.%) has a maximum adsorption capacity of 71.83 ± 2.03 mgg^{-1}. It has also been demonstrated that electrostatic interactions are responsible for the CR dye adsorption onto Sr-doped ZnO (15 wt. %). Temperature effects on CR dye adsorption suggest that the process is spontaneous adsorption and endothermic. An effective Sr-doped ZnO adsorbent was prepared using a simple co-precipitation procedure.

Conflicts of interest

The authors declare that they have no known competing financial interests or personal relationships that could have appeared to influence the work reported in this paper.

References

[1] Akhtar N, Syakir Ishak MI, Bhawani SA, Umar K. Various natural and anthropogenic factors responsible for water quality degradation: a review. Water (Switzerland) 2021;13: 2660–95.

[2] Sarker B, N. Keya K, I. Mahir F, M. Nahiun K, Shahida S, A. Khan R. Surface and ground water pollution: causes and effects of urbanization and industrialization in south asia. Guigoz Sci Rev 2021;73:32–41.

[3] Reddy IN, Reddy CV, Shim J, Akkinepally B, Cho M, Yoo K, et al. Excellent visible-light driven photocatalyst of (Al, Ni) co-doped ZnO structures for organic dye degradation. Catal Today 2020;340:277–85.

[4] Bensalah J, Habsaoui A, Dagdag O, Lebkiri A, Ismi I, Rifi EH, et al. Adsorption of a cationic dye (Safranin) by artificial cationic resins Amberlite®IRC-50: equilibrium, kinetic and thermodynamic study. Chemical Data Collections 2021;35: 100756–91.

[5] Bensalah J, Benhiba F, Habsaoui A, Ouass A, Zarrouk A, Lebkiri A, et al. The adsorption mechanism of the anionic and cationic dyes of the cationic resin A®IRC-50, kinetic study and theoretical investigation using DFT. J Indian Chem Soc 2022;99:100512–23.

[6] Amri A El, Bensalah J, Idrissi A, Lamya K, Ouass A, Bouzakraoui S, et al. Adsorption of a cationic dye (Methylene bleu) by Typha Latifolia: equilibrium, kinetic, thermodynamic and DFT calculations. Chemical Data Collections 2022;38:100834–52.

[7] El Kerdoudi Z, Bensalah J, Helli H, El mekkaoui A, EL Mejdoub N. Investigation of the cationic dye methylene blue in the treatment of wastewater clay from Sidi-Kacem (Morocco): kinetic and mathematical modelling of experimental data. Mater Today Proc 2023;72:3550–5.

[8] Bensalah J, Habsaoui A, Lebkiri A, El Khattabi O, Rifi EH. Investigation of the cationic resin Amberlite®IRC-50 as a potential adsorbent to remove the anionic dye methyl orange. Desalination Water Treat 2022;246:280–90.

[9] Bensalah J, Idrissi A, Faydy M El, Doumane G, Staoui A, Hsissou R, et al. Investigation of the cationic resin as a potential adsorbent to remove MR and CV dyes: kinetic, equilibrium isotherms studies and DFT calculations. J Mol Struct [Internet 2023;1278:134849–59.

[10] Katheresan V, Kansedo J, Lau SY. Efficiency of various recent wastewater dye removal methods: a review. J Environ Chem Eng 2018;6:4676–97.

[11] Srivatsav P, Bhargav BS, Shanmugasundaram V, Arun J, Gopinath KP, Bhatnagar A. Biochar as an eco-friendly and economical adsorbent for the removal of colorants (Dyes) from aqueous environment: a review. Water (Switzerland) 2020;12:3561–88.

[12] Toumi I, Djelad H, Chouli F, Benyoucef A. Synthesis of PANI@ZnO hybrid material and evaluations in adsorption of Congo red and methylene blue dyes: structural characterization and adsorption performance. J Inorg Organomet Polym Mater 2022;32:112–21.

[13] Harja M, Buema G, Bucur D. Recent advances in removal of Congo Red dye by adsorption using an industrial waste. Sci Rep 2022;12:6087–105.

[14] Simonescu CM, Tătăruş A, Culiţă DC, Stănică N, Ionescu IA, Butoi B, et al. Comparative study of cofe2o4 nanoparticles and cofe2o4-chitosan composite for Congo red and methyl orange removal by adsorption. Nanomaterials 2021;11: 711–35.

[15] Solayman HM, Hossen MA, Abd Aziz A, Yahya NY, Leong KH, Sim LC, et al. Performance evaluation of dye wastewater treatment technologies: a review. J Environ Chem Eng 2023;11:109610–35.

[16] Chikri R, Elhadiri N, Benchanaa M, El maguana Y. Efficiency of sawdust as low-cost adsorbent for dyes removal. J Chem 2020;2020:1–17.

[17] Lellis B, Fávaro-Polonio CZ, Pamphile JA, Polonio JC. Effects of textile dyes on health and the environment and bioremediation potential of living organisms. Biotechnology Research and Innovation 2019;3:275–90.

[18] Jayakumar J, Chou HH. Recent advances in visible-light-driven hydrogen evolution from water using polymer photocatalysts. ChemCatChem 2020;12:689–704.

[19] Yang Q, Song H, Li Y, Pan Z, Dong M, Chen F, et al. Flower-like core-shell Fe 3 O 4 @MnO 2 microspheres: synthesis and selective removal of Congo red dye from aqueous solution. J Mol Liq [Internet 2017;234:18–23.

[20] Zare K, Sadegh H, Shahryari-ghoshekandi R, Maazinejad B, Ali V, Tyagi I, et al. Enhanced removal of toxic Congo red dye using multi walled carbon nanotubes: kinetic, equilibrium studies and its comparison with other adsorbents. J Mol Liq [Internet 2015 Dec;212:266–71.

[21] Dutta S, Gupta B, Srivastava SK, Gupta AK. Recent advances on the removal of dyes from wastewater using various adsorbents: a critical review. Materials Advances 2021;2: 4497–531.

[22] Mella B, Barcellos BS de C, da Silva Costa DE, Gutterres M. Treatment of leather dyeing wastewater with associated process of coagulation-flocculation/adsorption/ozonation. Ozone Sci Eng 2018;40:133–40.

[23] Mousazadeh M, Alizadeh SM, Frontistis Z, Kabdaşlõ I, Karamati Niaragh E, Al Qodah Z, et al. Electrocoagulation as a promising defluoridation technology from water: a review of state of the art of removal mechanisms and performance trends. Water (Switzerland) 2021;13:656–85.

[24] Marson EO, de Paiva VAB, Gonçalves BR, Gomes Júnior O, Borges Neto W, Machado AEH, et al. Degradation of Direct Red 81 mediated by Fenton reactions: multivariate optimization, effect of chloride and sulfate, and acute ecotoxicity assessment. Environ Sci Pollut Control Ser 2017;24:6176–86.

[25] Ağtaş M, Yõlmaz Ö, Dilaver M, Alp K, Koyuncu İ. Hot water recovery and reuse in textile sector with pilot scale ceramic ultrafiltration/nanofiltration membrane system. J Clean Prod 2020;256:120359–71.

[26] Detho A, Daud Z, Rosli MA, Awang H, Ridzuan MB Bin. Review on COD and ammoniacal nitrogen removal from landfill leachate using low-cost adsorbent. J Air Waste Manag Assoc 2022;72:10–23.
[27] Ighalo JO, Omoarukhe FO, Ojukwu VE, Iwuozor KO, Igwegbe CA. Cost of adsorbent preparation and usage in wastewater treatment: a review. Cleaner Chem Eng 2022;3: 100042–52.
[28] Maroušek J, Marousková A, Periakaruppan R, Gokul GM, Anbukumaran A, Bohatá A, et al. Silica nanoparticles from coir pith synthesized by acidic sol-gel method improve germination economics. Polymers (Basel) 2022;14:266–78.
[29] Hamd A, Dryaz AR, Shaban M, Almohamadi H, Abu Al-Ola KA, Soliman NK, et al. Fabrication and application of zeolite/acanthophora spicifera nanoporous composite for adsorption of Congo red dye from wastewater. Nanomaterials 2021;11:2441–61.
[30] Wang Y, Jiang F, Chen J, Sun X, Xian T, Yang H. In situ construction of CNT/cus hybrids and their application in photodegradation for removing organic dyes. Nanomaterials 2020;10:178–97.
[31] Beker SA, Khudur LS, Cole I, Ball AS. Catalytic degradation of methylene blue using iron and nitrogen-containing carbon dots as Fenton-like catalysts. New J Chem 2022;46: 263–75.
[32] Maroušek J, Trakal L. Techno-economic analysis reveals the untapped potential of wood biochar. Chemosphere 2022;291: 133000–11.
[33] Dehmani Y, Lgaz H, Alrashdi AA, Lamhasni T, Abouarnadasse S, Chung IM. Phenol adsorption mechanism on the zinc oxide surface: experimental, cluster DFT calculations, and molecular dynamics simulations. J Mol Liq 2021;324: 114993–5002.
[34] Huy NN, Thanh Thuy VT, Thang NH, Thuy NT, Quynh LT, Khoi TT, et al. Facile one-step synthesis of zinc oxide nanoparticles by ultrasonic-assisted precipitation method and its application for H2S adsorption in air. J Phys Chem Solid 2019;132:99–103.
[35] Safwat SM, Medhat M, Abdel-Halim H. Adsorption of phenol onto aluminium oxide and zinc oxide: a comparative study with titanium dioxide. Separ Sci Technol 2019;54: 2840–52.
[36] Phan DN, Rebia RA, Saito Y, Kharaghani D, Khatri M, Tanaka T, et al. Zinc oxide nanoparticles attached to polyacrylonitrile nanofibers with hinokitiol as gluing agent for synergistic antibacterial activities and effective dye removal. J Ind Eng Chem 2020;85:258–68.
[37] Nakarmi A, Bourdo SE, Ruhl L, Kanel S, Nadagouda M, Kumar Alla P, et al. Benign zinc oxide betaine-modified biochar nanocomposites for phosphate removal from aqueous solutions. J Environ Manag 2020;272:111048–60.
[38] Albadarin NA, Takriff MS, Salehmin MNI, Yin WW, Tan ST, Kadhum AAH, et al. Hydrothermal synthesis of Ag–ZnO nanostructures as an advanced material for photoelectrochemical applications. Int J Electrochem Sci [Internet 2021;16:1–11.
[39] Gerbreders V, Krasovska M, Sledevskis E, Gerbreders A, Mihailova I, Tamanis E, et al. Hydrothermal synthesis of ZnO nanostructures with controllable morphology change. CrystEngComm 2020;22:1346–58.
[40] Rath PP, Behera SS, Priyadarshini B, Panda SR, Mandal D, Sahoo T, et al. Influence of Mg doping on ZnO NPs for enhanced adsorption activity of Congo Red dye. Appl Surf Sci 2019;491:256–66.
[41] Ansari MS, Banik A, Kalita A, Iyer PK, Qureshi M. Multifunctional hierarchical 3-D ZnO superstructures directly grown over FTO glass substrates: enhanced photovoltaic and selective sensing applications. J Mater Chem A Mater 2018;6:15868–87.
[42] Ikram M, Aslam S, Haider A, Naz S, Ul-Hamid A, Shahzadi A, et al. Doping of Mg on ZnO nanorods demonstrated improved photocatalytic degradation and antimicrobial potential with molecular docking analysis. Nanoscale Res Lett 2021;16:78–94.
[43] Singh V, Gupta M. Characterisation and zeta potential measurements of CuO–water nanofluids. In: Lecture notes in mechanical engineering. Pleiades Publishing system; New York, USA: 2019. p. 741–7.
[44] Elmorsi TM, Elsayed MH, Bakr MF. Enhancing the removal of methylene blue by modified ZnO nanoparticles: kinetics and equilibrium studies. Can J Chem 2017;95:590–600.
[45] Gajewska M, Skrzypiec K, Jóźwiakowski K, Mucha Z, Wójcik W, Karczmarczyk A, et al. Kinetics of pollutants removal in vertical and horizontal flow constructed wetlands in temperate climate. Sci Total Environ 2020;718: 137371–80.
[46] Shaban M, AbuKhadra MR, Nasief FM, Abd El-Salam HM. Removal of ammonia from aqueous solutions, ground water, and wastewater using mechanically activated clinoptilolite and synthetic zeolite-A: kinetic and equilibrium studies. Water Air Soil Pollut 2017;228:450–66.
[47] Wang C, Liu K, Wang D, Wang G, Chu PK, Meng Z, et al. Hierarchical CuO–ZnO/SiO2 fibrous membranes for efficient removal of Congo red and 4-nitrophenol from water. Advanced Fiber Materials 2022;4:1069–80.
[48] Kouotou D, Gharibi EK, Bailón-García E, Ghalit M. Improved Cd (II) ions removal performance from aqueous solution using cerium doped activated carbon. Mater Today Proc 2022;51:1957–65.
[49] Elsayed MH, Elmorsi TM, Abuelela AM, Hassan AE, Alhakemy AZ, Bakr MF, et al. Direct sunlight-active Na-doped ZnO photocatalyst for the mineralization of organic pollutants at different pH mediums. J Taiwan Inst Chem Eng 2020;115:187–97.
[50] Shkir M, Al-Shehri BM, Pachamuthu MP, Khan A, Chandekar K v, AlFaify S, et al. A remarkable improvement in photocatalytic activity of ZnO nanoparticles through Sr doping synthesized by one pot flash combustion technique for water treatments. Colloids Surf A Physicochem Eng Asp 2020;587:124340–9.
[51] Yarahmadi M, Maleki-Ghaleh H, Mehr ME, Dargahi Z, Rasouli F, Siadati MH. Synthesis and characterization of Sr-doped ZnO nanoparticles for photocatalytic applications. J Alloys Compd 2021;853:157000–14.
[52] Singh V, Kumar A, Alam M, Kumar A, Kumar P, Goyat V. A study of morphology, UV measurements and zeta potential of Zinc Ferrite and Al2O3 nanofluids. Mater Today Proc 2022;59:1034–9.
[53] de Souza EF, Appel LG. Oxygen vacancy formation and their role in the CO2 activation on Ca doped ZrO2 surface: an ab-initio DFT study. Appl Surf Sci 2021;553:149589–602.
[54] Abdi J, Vossoughi M, Mahmoodi NM, Alemzadeh I. Synthesis of metal-organic framework hybrid nanocomposites based on GO and CNT with high adsorption capacity for dye removal. Chem Eng J 2017;326:1145–58.
[55] Xiao W, Jiang X, Liu X, Zhou W, Garba ZN, Lawan I, et al. Adsorption of organic dyes from wastewater by metal-doped porous carbon materials. J Clean Prod 2021;284: 124773–93.
[56] Khumalo SPG, Lokhat D, Chetty K, Chetty L. Synthesis of novel carbon-supported iron oxide sorbents for adsorption of dye from aqueous solutions: equilibrium and flow-through studies. Sci Rep 2022;12:20009–25.
[57] Alshabanat MN, Al-Anazy MM. An experimental study of photocatalytic degradation of Congo red using polymer nanocomposite films. J Chem 2018;2018:1–8.
[58] Litefti K, Freire MS, Stitou M, González-Álvarez J. Adsorption of an anionic dye (Congo red) from aqueous solutions by pine bark. Sci Rep 2019;9:16530–41.
[59] Shaban M, Abukhadra MR. Geochemical evaluation and environmental application of Yemeni natural zeolite as

sorbent for Cd2+ from solution: kinetic modeling, equilibrium studies, and statistical optimization. Environ Earth Sci 2017;76:310−26.
[60] Zhang L, Loáiciga HA, Xu M, Du C, Du Y. Kinetics and mechanisms of phosphorus adsorption in soils from diverse ecological zones in the source area of a drinking-water reservoir. Int J Environ Res Publ Health 2015;12:14312−26.
[61] Farghali MA, Selim AM, Khater HF, Bagato N, Alharbi W, Alharbi KH, et al. Optimized adsorption and effective disposal of Congo red dye from wastewater: hydrothermal fabrication of MgAl-LDH nanohydrotalcite-like materials. Arab J Chem 2022;15:104171−83.
[62] Yan X, Zhang X, Li Q. Preparation and characterization of CS/β-CD/Nano-ZnO composite porous membrane optimized by Box-Behnken for the adsorption of Congo red. Environ Sci Pollut Control Ser 2018;25:22244−58.
[63] Zheng Y, Wang H, Cheng B, You W, Yu J. Fabrication of hierarchical bristle-grass-like NH4Al(OH)2CO3@Ni(OH)2 core-shell structure and its enhanced Congo red adsorption performance. J Alloys Compd 2018;750:644−54.
[64] Lafi R, Montasser I, Hafiane A. Adsorption of Congo red dye from aqueous solutions by prepared activated carbon with oxygen-containing functional groups and its regeneration. Adsorption Science & Technology [Internet] 2019;37:160−81.